SPECIAL ISSUE ARTICLE

Applied
Ceramic
TECHNOLOGY
International Journal of

Reticulated ceramic foams from alumina-chromia solid solutions: A feasibility study

Ulf Betke | **Daniel Schrake** | **Michael Scheffler**

Otto-von-Guericke University Magdeburg, Institute for Materials and Joining Technology, Magdeburg, Germany

Correspondence

Michael Scheffler, Otto-von-Guericke University Magdeburg, Institute for Materials and Joining Technology, Universitaetsplatz 2, 39106 Magdeburg, Germany.
Email: m.scheffler@ovgu.de

Abstract

Open cellular ceramic foams were manufactured from plain and chromia-doped alumina, with a chromium concentration ranging between 1.25 mol% and 5.0 mol%. The $(AlCr)_2O_3$ starting powders were prepared by precipitation of a chromia precursor onto the surface of an alumina powder and subsequent calcination. Characterization of the starting powders as well as the foam samples made therefrom were carried out with respect to the chromium concentration in the alumina phase and the influence of the dopant on the cellular structure and sintering behavior of the doped material. While no positive effect on the compressive strength of the ceramic foams was found, the dopant influences the sintering behavior resulting in an increased shrinkage and in a reduction of total porosity.

KEYWORDS

chromia-alumina solid solution, reticulated ceramic foams

1 | INTRODUCTION

Open-cellular ceramic foams have been manufactured from a great variety of materials, among them from alumina.[1,2] Applications may be found as molten metal filters, as supports for solid-particle catalysts and heat storage materials, or for light metal reinforcement.[3–5] Topical research in this field is mainly dedicated to surface area enlargement, surface modification with a second phase or increase of the foam´s mechanical strength.[6–16]

In this study, we aim to introduce chromia into alumina: chromia—Cr_2O_3—and alumina—Al_2O_3—form a solid solution with indefinite miscibility at temperatures above 1200°C (Figure 1; Ref. 17). At lower temperatures, a (pressure dependent) miscibility gap exists, which may result in a phase separation into two individual corundum phases. The ionic radii of Al^{3+} (54 pm) and Cr^{3+} (62 pm) differ by 15%[18]; thus, incorporation of Cr^{3+} into alumina

results in a change of the electronic properties by compression of the 3d orbitals of chromium.[19] Most evidently, this expresses in a shift of the optical absorption maximum for Cr^{3+} from red to green and consequently in a color change: Whereas pure alumina is colorless and pure chromia is green, $(AlCr)_2O_3$ solid solutions with a few percent Cr^{3+} are of intense red color (ruby). Besides the optical effects, the Cr^{3+} doping is expected to affect the mechanical characteristics of the respective ceramic composites. The larger size of Cr^{3+} compared to Al^{3+} may lead to residual stresses in the crystal lattice, when only part of Al^{3+} is substituted by Cr^{3+}. These stresses might be similar to the compressive stresses which are generated in Al_2O_3-ZrO_2 transformation toughened ceramic composites[20–23] and might result in an increase in strength for the Cr^{3+}-doped alumina ceramics. Therefore, the main focus of the present study is the preparation of cellular ceramics made of chromium-doped alumina and the investigation

of the compressive strength under consideration of microstructural effects and the crystal chemical characteristics of the $(AlCr)_2O_3$ solid solution phase(s).

For this purpose, a precipitation route was selected for the starting powder synthesis. The chromia precursor $(NH_4)Cr(OH)_2(CO_3)$ was precipitated in varying amounts onto the surface of a conventional alumina ceramic powder and converted into Cr_2O_3 by calcination at 1000°C. In Figure 1, the composition of the respective samples is shown in the context of the phase diagram of Al_2O_3–Cr_2O_3. From the obtained starting powders, dispersions suitable for the Schwartzwalder polymer foam replication process [24] were prepared from which the respective cellular ceramics were manufactured. Characterization of composite powders and foams was conducted by powder X-ray
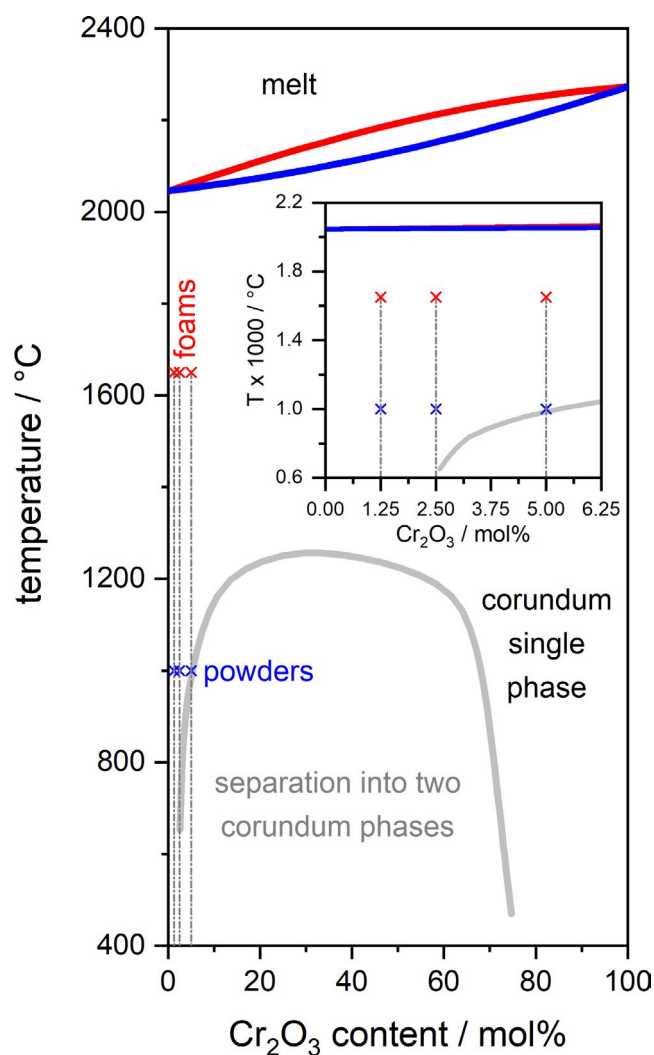
diffraction (pXRD) and Rietveld analysis with respect to the chromium concentration and phase composition. For the obtained ceramic foams, the porosity was analyzed by the Archimedes principle as well as microcomputed tomography (μ-CT). In addition, the compressive strength was measured and the obtained data were correlated to the sample's microstructure.

2 | EXPERIMENTAL PROCEDURE

2.1 | Starting materials preparation

The chromium-doped alumina powders as starting materials for the foam manufacturing were prepared by precipitation of the Cr_2O_3 precursor compound $(NH_4)Cr(OH)_2(CO_3)$ onto alumina particles followed by a calcination procedure. The precipitation of the $(NH_4)Cr(OH)_2(CO_3)$ precursor was adapted from Ref. 25

The typical procedure was as follows (given amounts of reactants refer to the $(AlCr)_2O_3$ powder containing 1.25 mol% Cr; Table 1 summarizes the reactant amounts for all samples): 204 g (2.00 mol Al_2O_3; 4.00 mol Al^{3+}) of alumina powder (CT 3000 SG; Almatis GmbH, Ludwigshafen, Germany; $d_{50} = 0.5$ μm) was dispersed in 400 mL deionized water. The dispersion was heated to 60°C; subsequently, 20.24 g (50.6 mmol) of chromium(III)-nitrate nonahydrate $(Cr(NO_3)_3 \cdot 9H_2O$; Acros Organics, New Jersey, USA) was dissolved in the alumina dispersion under vigorous stirring. The obtained dispersion is referred to as dispersion A. Separately, 14.57 g (151.8 mmol; 3 eq. w. r. t. $Cr(NO_3)_3 \cdot 9H_2O)$ of ammonium carbonate $((NH_4)_2CO_3$; Sigma Aldrich, Darmstadt, Germany) was dissolved in 76 ml deionized water, so that a solution with 2 mol L^{-1} ammonium carbonate was obtained. This is solution B. Finally, the $(NH_4)_2CO_3$ solution B was added dropwise to the $Al_2O_3/Cr(NO_3)_3$ mixture A using a dropping funnel with a rate of 1 drop per second. The dispersion was maintained at 60°C and stirred vigorously during

FIGURE 1 Phase diagram Al_2O_3-Cr_2O_3 and composition of the composite powders (calcined at 1000°C) and foams (sintered at 1650°C) prepared within this work. The phase diagram is redrawn using data published in Ref. 17 The inset shows the region investigated within this work

TABLE 1 Composition for the $(NH_4)Cr(OH)_2(CO_3)$ precipitation on alumina; solution B was added dropwise to dispersion A. theoretical Cr^{3+} concentrations were 1.25 mol%, 2.5 mol%, and 5.0 mol%

		Composition // mol% Cr^{3+} in $(AlCr)_2O_3$		
Component		**1.25**	**2.5**	**5.0**
A	Demineralized H_2O / ml	400	400	400
	Alumina CT 3000 SG / g	204.0	204.0	204.0
	$Cr(NO_3)_3 \cdot 9H_2O$ / g	20.24	41.20	84.40
B	Demineralized H_2O / ml	76	155	317
	$(NH_4)_2CO_3$ / g	14.57	29.66	60.77

the addition. The whole process took approximately 30–120 minutes, depending on the amount of solution. After addition of the ammonium carbonate solution the resulting solid was separated from the aqueous solution by filtration. In order to remove excess $(NH_4)_2CO_3$ as well as formed $(NH_4)NO_3$, the collected powders were redispersed in 500 ml demineralized water. The mixture was heated to 80°C and stirred vigorously for 2 h. Afterward, all solids were again collected by filtration. The washing procedure was repeated until the washing solution was almost free of carbonate and nitrate salts, which can be controlled by simple density determination. A thorough washing of the $(NH_4)Cr(OH)_2(CO_3)@Al_2O_3$ powder is necessary to avoid oxidation of Cr^{3+} during the final calcination step by residual nitrate salts.

After drying at ambient conditions, the precursor powders were transferred into an alumina dish, which was additionally loaded with a second (smaller) alumina boat containing 3.0 g carbon fibers. The carbon fibers are added for consuming the oxygen being present in the reaction vessel and to provide a slightly reducing CO/CO_2 atmosphere in order to avoid oxidative loss of Cr in the form of CrO_3. The entire setup was sealed with a chamotte lid with a mineral wool mat in between to close an eventual gap between the alumina dish and chamotte lid. Calcination was carried out in a chamber furnace (Nabertherm LH 30/14, Nabertherm GmbH) at 1000°C with a heating rate of 5 K min^{-1}, a holding time at a peak temperature of 3 h and a cooling rate to room temperature of 5 K min^{-1}. After the withdrawal of the powders from the furnace they were ball-milled in ethanol—150 ml ethanol, 130 g of doped alumina powder, and 50 alumina balls with a diameter of 10 mm in a 250 mL alumina grinding bowl—using a planetary ball mill (PM 400, Retsch Technology GmbH). The ball mill was operated for 1 hour at a rotational speed of 300 revelations per minute. After milling, the $(AlCr)_2O_3$ powders were sieved and mortared and used for ceramic foam preparation. The proof of chromium incorporation in alumina was carried out by X-ray powder diffraction analysis (pXRD) combined with Rietveld analysis for phase amount detection as will be described below.

2.2 | Dispersion formulation and foam manufacturing

Ceramic foams from the Cr^{3+} doped alumina powders were manufactured according to Ref. 26 The ethylammonium citrate deflocculant Dolapix CE 64, the polyvinylalcohol binder Optapix PA 4G and the de-foaming agent Contraspum K 1012 used as processing aids were obtained from Zschimmer & Schwarz GmbH & Co. KG. Table 2 provides the composition of the respective dispersions.

The solid load of the dispersions was 78.3% for the undoped powder, 78.4%, 72.8%, and 77.5% for the dispersions

TABLE 2 Dispersion compositions used for the $(AlCr)_2O_3$ foam manufacturing

Component / g	Sample series // mol% Cr^{3+} in $(AlCr)_2O_3$			
	0.0	**1.25**	**2.5**	**5.0**
Dolapix CE 64	1.00	1.00	1.00	1.00
Demineralized H_2O	25.0	25.0	34.3	26.5
Alumina, undoped	100.0	—	—	—
Alumina, Cr-doped	—	100.0	100.0	100.0
Optapix PA 4G	1.50	1.50	1.50	1.50
Contraspum K 1012	0.10	0.10	0.10	0.10
Total solid content / wt%	78.3	78.4	72.8	77.5

with the Cr-doped powders (in ascending sequence w. r. t. the doping amount). The dispersion preparation was performed using a planetary centrifugal mixer (Thinkymixer ARE-250, THINKY Corp.) according to a previously described procedure.[26] The $(AlCr)_2O_3$ ceramic foams were prepared by coating the obtained dispersions onto polyurethane (PU) foam templates with 20 pores per inch (ppi). The template foams (SP30P20R, Koepp Schaum GmbH) were of circular shape with 30 mm in height and 20 mm in diameter. The templates were coated with the respective dispersion according to the procedure described in Ref. 26 Depending on the solid load of the dispersion, the PU foam templates were loaded with 2.8 g to 3.2 g of the $(AlCr)_2O_3$ dispersion, which corresponds to a total porosity of approx. 90% after final sintering.

After drying, the thermal removal of the PU templates was carried out with a heating rate of 3 K min^{-1} to 650°C and a dwell time of 3 h followed by a pre-sintering step at 1,350°C and a heating rate of 3 K min^{-1}; the dwell time was 3 hours and the cooling rate was set to 10 K min^{-1}. After this pre-sintering step, the foams were transferred to a high-temperature furnace and sintered at 1650°C for 3 hours. Heating and cooling rates were set to 3 K min^{-1} and 10 K min^{-1}, respectively. For the template burnout and the sintering procedure, the foam samples were placed in an upright position (on the circular base area).

Powder samples after doping and calcination at 1,000°C are assigned as Al_2O_3-P-x.xx, and foam samples with a peak sintering temperature of 1650°C are assigned as Al_2O_3-F-x.xx; x.xx reflects the Cr^{3+} concentration in mol%.

2.3 | Characterization of powder and foam samples

The $(AlCr)_2O_3$ powders were characterized with respect to the phase composition and the incorporation of Cr^{3+}; X-ray diffraction analysis was carried out with a D8 Discover

(Bruker-AXS GmbH) with Bragg–Brentano reflection geometry in a 2θ range from 20° to 160° and Co $K\alpha_{1/2}$ radiation. The X-ray tube was operated with 35 kV and 40 mA, a fixed divergence slit of 0.6 mm, 2.5° primary and secondary soller slits were used as optical components. The diffracted intensities were recorded using a Lynxeye XE-T energy-dispersive detector operated in 1D mode using the whole detector area for counting. With the help of the TOPAS Academic V5 software package for Rietveld analysis, the phase compositions were determined. The Cr^{3+} concentration in the ceramic powders was calculated by Vegard's law from the unit cell volume of the respective $(AlCr)_2O_3$ corundum phase(s) under consideration of data from Ref. 27.

The foams were characterized with respect to their sintering and shrinkage behavior, porosity, phase composition (pXRD), Cr^{3+} concentration (pXRD), and compressive strength. The phase composition and Cr^{3+} incorporation were determined as described for the powders; the foams were milled in a mortar prior to characterization with pXRD. A complementary approach for the proof of the Cr^{3+} incorporation into the corundum phase of the foam strut material was carried out with Raman spectroscopy. Powders were analyzed with an Alpha 300R Raman microscope (WITec GmbH) equipped with a 55 mW laser with an excitation wavelength of 532 nm; the scattered light was recorded in a wavenumber range between 4000 cm^{-1} and 5000 cm^{-1} being equivalent to a wavelength of 676 nm to 725 nm.

The porosity was determined with respect to the total (geometric) porosity from the foam weight and the geometric volume. The strut porosity, being comprised of the hollow strut cavities and the strut material pores was measured by the Archimedes' principle according to the DIN EN 623-2:1993-11 standard.[28] At least ten specimens per sample series were analyzed and the results were averaged. For details on the porosity measurements, see Refs.[6,16].

The cell size of the foams was determined with a microcomputer tomograph (nanotom S, GE Sensing & Inspection Technologies, Wunstorf, Germany) and the software CTAnalyser V.1.18 (Bruker microCT, Kontich, Belgium) for analysis of the tomographic data. The X-ray source was operated at 60 kV and 160 µA, and no further filtering has been applied. The voxel size was adjusted to a resolution of $(12 \, \mu m)^3$ which allows the analysis of a $(27 \, mm)^3$ section of the respective foam sample. The reconstruction of the 3D sample volume was performed with the datos|X 2.0 software GE Sensing & Inspection Technologies). The cell size of the respective foam samples was detrrmined from the binarized tomographic data by morphometric calculations in the CTAnalyser software. For binarization, the differential thresholding approach was used. Prior to the morphometric analyses, a despeckling was applied to the data. For further details of the tomographic characterization and the morphology analysis using CTAnalyser, please see Refs. 10,29.

The compressive strength of the foams was determined with a TIRATEST 2825 universal testing machine (TIRA GmbH, Schalkau, Germany) equipped with two circular loading plates of 150 mm in diameter. The foam specimens were mounted within the testing machine in between two cardboard pieces for ensuring a more homogeneous loading of the samples. The measurement was performed at a crosshead speed of 1 mm mm^{-1}. The maximum force was extracted from the data and used for the calculation of the compressive strength. At least 10 specimens were measured per sample series and the average compressive strength was calculated using the 2-parameter Weibull distribution as implemented in the Visual-XSel 14 software.[30]

3 | RESULTS AND DISCUSSION

3.1 | Preparation and characterization of the $(AlCr)_2O_3$ powders

During the addition of the ammonium carbonate solution to the alumina/$Cr(NO_3)_3$ mixture, a change in color was observed from violet (color of the $Cr(H_2O)_6]^{3+}$ complex cation) to almost colorless. After filtration, a clear and colorless filtrate as well as a pale violet precipitate were obtained. This indicates quantitative precipitation of the Cr_2O_3 precursor compound $(NH_4)Cr(OH)_2(CO_3)$ under the chosen reaction conditions.

For the calcination of the $(NH_4)Cr(OH)_2(CO_3)$@alumina powder in order to obtain the desired $(AlCr)_2O_3$ solid solution, the importance of a thorough washing of the precipitate has been manifested. The oxidation reaction of Cr(III) into Cr(VI) is favored under alkaline conditions[19]; thus, remaining carbonate and nitrate salt contaminations result in the formation of Cr(VI) compounds. In preliminary experiments, the formation of Cr(VI) species during the calcination at 1,000°C has been observed for powders, which were washed only once. Hexavalent chromium is carcinogenic on the one hand side, and the formation of volatile CrO_3 lowers the effective chromium content in the corundum phase. Thus, a proper washing procedure after the precipitation reaction is highly recommended. The density measurement of the washing solution is a valid indicator; washing has been repeated until the density of the washing solution was constant (and close to ≈ 1.0 g mL^{-1} for water). For this, 2–3 washing cycles were necessary, depending on the Cr content in the precursor powders.

After calcination, the $(AlCr)_2O_3$ powders Al_2O_3-P-1.25 and Al_2O_3-P-2.5 with a Cr^{3+} concentration of 1.25 mol% and 2.5 mol%, respectively, show a light reddish shade, whereas the powder with 5.0 mol% Cr^{3+} is pale green (Figure 2). This suggests the complete incorporation of all Cr^{3+} into the corundum lattice of alumina for the powders with 1.25 mol% Cr^{3+} and 2.5 mol% Cr^{3+}, respectively. The Cr^{3+} concentration in

these samples is clearly below the miscibility gap in the system Al_2O_3-Cr_2O_3, see alsoFigure 1.[17] Thus, the formation of a homogeneous solid solution is expected at a calcination temperature of 1,000°C. In contrast, thereto, the powder with 5.0 mol% Cr^{3+} most likely contains phases with significantly higher Cr^{3+} concentration, which are expected to be of green color.

According to pXRD and Rietveld analysis, the samples Al_2O_3-P-1.25 and Al_2O_3-P-2.5 consist of two individual corundum phases, no other ternary Al-Cr oxides were observed (Figure 3). This becomes apparent in the splitting of the reflections, especially at higher diffraction angles. In both samples, one phase is pure alumina with a corundum structure and a cell volume of 255.02 $Å^3$ and 255.09 $Å^3$, respectively. For the second corundum phase an increased cell volume of 256.52 $Å^3$ and

FIGURE 2 $(AlCr)_2O_3$ powders obtained after calcination at 1000°C with 1.25 mol% Cr^{3+} (left), 2.5 mol% Cr^{3+} (middle) and 5.0 mol% Cr^{3+} (right)

257.97 $Å^3$, respectively, was obtained from the Rietveld analysis. This volume expansion of the unit cell is a result of the incorporation of the 15% larger Cr^{3+} ions (61.5 pm vs. 53.5 pm for Al^{3+}; ref. [18]) into the corundum structure. The phase composition is equal in the samples Al_2O_3-P-1.25 and Al_2O_3-P-2.5 with 78 wt% of pure alumina and 22 wt% of the $(AlCr)_2O_3$ phase with increased unit cell volume (Table 3).

A linear correlation between the unit cell volume of Cr-doped corundum and the Cr^{3+} concentration according to Vegard's law [31] has already been confirmed in the literature.

From this regression function the Cr^{3+} content in a given corundum phase can be estimated according to Equation 1:

$$x_{Cr} = (V - 255.07 Å^3)/0.3507 \quad mol\% Å^{-3} \qquad (1)$$

For the samples Al_2O_3-P-1.25 and Al_2O_3-P-2.5, a Cr^{3+} concentration in the $(AlCr)_2O_3$ solid solution phase of 4.1 mol% and 10.9 mol%, respectively, is the result.

The phase composition of the Al_2O_3-P-5.0 powder is of higher complexity. In total, four different corundum phases were identified in the pXRD pattern by a profile analysis of the observed reflections. According to a Rietveld analysis, one corundum phase is pure alumina (68 wt%) and three $(AlCr)_2O_3$ solid solution phases co-exist: a) 4.4 wt% with 83.9 mol% Cr^{3+}, b) 9.0 wt% with 22.2 mol% Cr^{3+}, and c) 18.4 wt% with 3.1 mol% Cr^{3+}. The $(AlCr)_2O_3$ phase a) is considered as Al^{3+}-doped chromia and thus expected to cause the green color of the sample Al_2O_3-P-5.0.

Finally, under consideration of the relative phase content of the pure alumina as well as $(AlCr)_2O_3$ solid solution phases, a total Cr^{3+} concentration of 0.75 mol%, 2.07 mol%, and 4.89 mol%, respectively, can be calculated for the samples Al_2O_3-P-1.25, Al_2O_3-P-2.5, and Al_2O_3-P-5.0. For the
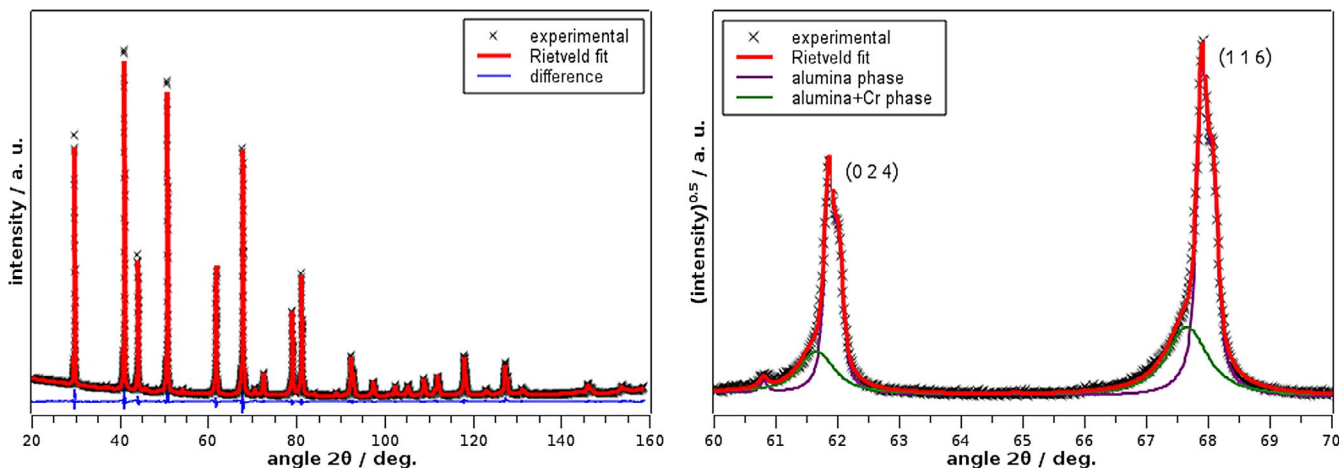
FIGURE 3 pXRD measurement and Rietveld analysis for an $(AlCr)_2O_3$ powder with 2.5 at.% Cr^{3+} calcined at 1000°C (left). The detail plot (right) shows the splitting of the reflections due to the presence of two individual corundum phases (violet and green line) with slightly different lattice constants. As an example, the (0 2 4) and (1 1 6) reflections are shown, the splitting is observed for all other reflections as well

Sample	Cell volume / $Å^3$	Phase content / wt%	Cr^{3+} content phase / at.%	Total Cr^{3+} content sample / at.%
Al_2O_3-P-1.25	255.02	78.4	0	0.75
	256.52	21.6	4.1	
Al_2O_3-P-2.5	255.09	77.8	0	2.07
	257.97	22.2	10.9	
Al_2O_3-P-5.0	255.03	68.2	0	4.89
	284.49	4.4	83.9	
	262.88	9.0	22.2	
	256.12	18.4	3.1	
Al_2O_3-F-1.25	255.33	100	0.82	0.82
Al_2O_3-F-2.5	255.76	100	2.02	2.02
Al_2O_3-F-5.0	256.73	100	4.79	4.79

TABLE 3 Cr^{3+} concentration in ceramic powders after calcination at 1,000°C and in ceramic foams made therefrom after sintering at 1,650°C; phase compositions determined by Rietveld technique and the Cr^{3+} concentration calculated by Vegard's law with the unit cell volume and lattice constant data from Ref. [27]
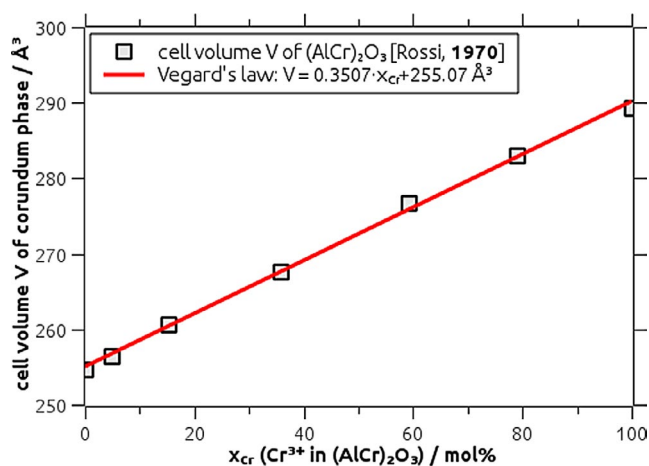

FIGURE 4 Regression analysis of the cell volume / Cr^{3+} concentration data for $(AlCr)_2O_3$ solid solutions adapted from Ref. 27 The regression function is applied for the estimation of the Cr^{3+} content in the samples within this work

powders Al_2O_3-P-1.25 and Al_2O_3-P-2.5, this is only 60% and 83% of the intended Cr^{3+} content of 1.25 mol% and 2.5 mol%, whereby for the Al_2O_3-P-5.0 specimen the intended Cr^{3+} is almost reached. The reason for this deficiency is not clear yet, probably it is due to the limited accuracy of the Rietveld technique for the quantitative phase analysis (Figure 4).

The formation of several co-existing corundum phases with different lattice parameters and therefore varying Cr^{3+} concentration indicates a slow diffusion of Cr^{3+} (and Al^{3+}) within the oxide phases. This is a consequence of the low calcination temperature of 1000°C. In this context, the approximation of the experimental powder pattern using the Rietveld technique and a set of corundum phases with slightly different lattice constants should be considered as an approximation of the true sample microstructure. In reality, the Cr^{3+} concentration will follow a more or less continuous gradient from the particle surface to the core resulting in continuously transforming lattice parameters. However, this behavior cannot be analyzed by the Rietveld approach, as it needs phases with a distinct set of lattice parameters. Nevertheless, the approach using a finite number of corundum phases with slightly different lattice constants gives a realistic estimate of the total Cr^{3+} concentration within the material as the results obtained for the multiphase powders processed at 1.000°C are in good agreement with the finally sintered foam struts, which consist of a single corundum solid solution phase without a detectable Cr^{3+} gradient (Table 3).

Before calcination, the powder particles can be described by means of a core-shell structure (Figure 5), whereas $(NH_4)Cr(OH)_2(CO_3)$, as precipitated on the CT 3000 SG particles, represents the shell. During calcination, $(NH_4)Cr(OH)_2(CO_3)$ decomposes into finely divided Cr_2O_3 which then starts to form a solid solution on the surface of the alumina core of the particles. Depending on the amount of Cr_2O_3 and the diffusion coefficients of Cr^{3+} and Al^{3+}, the concentration gradient between the surface and bulk volume of the particles is expected to decrease during the calcination process. Nevertheless, the temperature of 1,000°C is too low for obtaining a homogeneous $(AlCr)_2O_3$ solid solution. For instance, the Cr-Al interdiffusion in the related spinel compound $MgAl_{0.4}Cr_{1.6}O_4$, is slow for temperatures below 1,500°C with an interdiffusion coefficient $D_{Cr-Al} \approx 1.0 \cdot 10^{-12}$ cm^2 s^{-1}.[32] For 1700°C, D_{Cr-Al} increases by two orders of magnitude to $1.1 \cdot 10^{-10}$ cm^2 s^{-1}. Thus, homogenization of the Cr distribution in the $(AlCr)_2O_3$ samples within this work is expected for the (foam) samples finally sintered at 1650°C.

3.2 | Preparation and characterization of the $(AlCr)_2O_3$ ceramic foams

For all prepared $(AlCr)_2O_3$ powders, the formulation of a suitable dispersion for the manufacturing of ceramic foams by the Schwartzwalder sponge replication process was
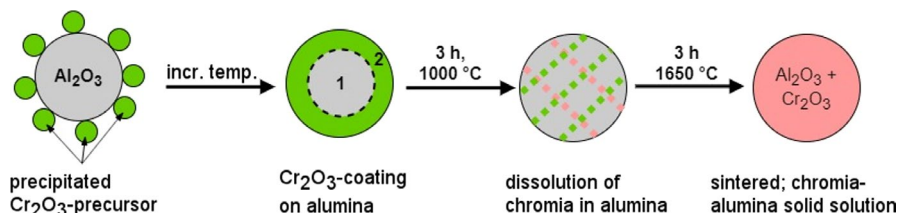
FIGURE 5 Schematic representation of the Cr^{3+} incorporation into alumina after chromia precipitation and temperature increase during calcination and final sintering
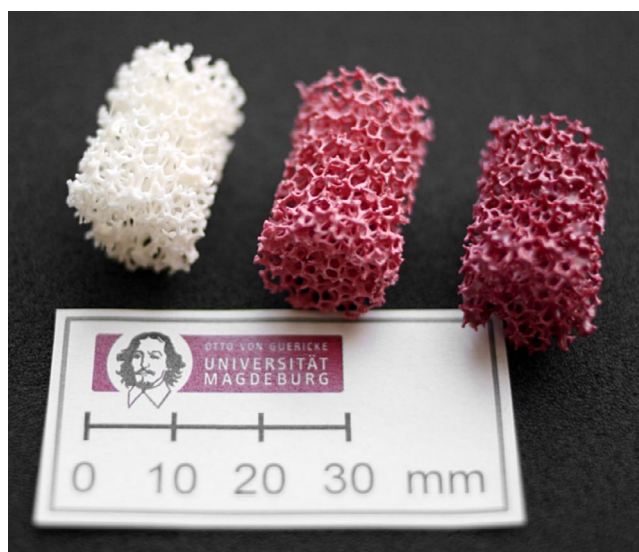

FIGURE 6 Ceramic foams manufactured from different corundum powders and finally sintered at 1,650°C: pure alumina (left), $(AlCr)_2O_3$ with 1.25 mol% Cr^{3+} (middle) and $(AlCr)_2O_3$ with 2.5 mol% Cr^{3+} (right). The foam sample with 5.0 mol% is not shown
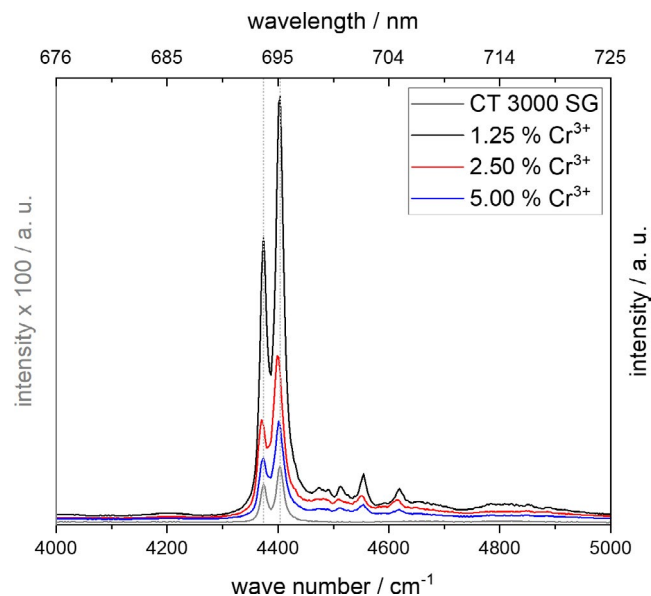

FIGURE 7 Raman spectra in the NIR range showing the red luminescence of Cr^{3+} incorporated into the alumina lattice; excitation wavelength was 532 nm

possible. In general, it should be noted that the viscosity of the $(AlCr)_2O_3$ dispersions was higher in comparison to pure CT 3000 SG alumina powder dispersions at the same solid load. Most likely, this is a consequence of finely divided $(AlCr)_2O_3$ powder fractions formed during the calcination and ball mill processing. Thus, the solid content in the respective dispersions had to be decreased by visual judgment with respect to the flow characteristics of the dispersion.

After the final sintering step, all $(AlCr)_2O_3$ solid solution foams possessed the characteristic red color of Cr-doped alumina ("ruby"), whereas an increase in color intensity was noticed for an increasing Cr^{3+} concentration from 1.25 mol% to 5.0 mol% (Figure 6).

Raman spectroscopic investigation of strut cross sections confirmed the homogeneous dissolution of Cr^{3+} into alumina. In Figure 7 Raman spectra in the NIR range of a pure alumina reference sample as well as $(AlCr)_2O_3$ foams with a Cr^{3+} amount of 1.25 mol%, 2.5 mol%, and 5 mol%

are presented. All samples show the red luminescence signal (double peak at 693 nm and 695 nm) characteristic for Cr^{3+} ions in an octahedral environment within the alumina lattice.[33] Interestingly, the pure alumina foam shows a luminescence signal of low intensity as well, which was assigned to Cr^{3+} impurities in the CT 3000 SG powder. Moreover, it was observed that the luminescence intensity of the $(AlCr)_2O_3$ foam strut material decreased with increasing concentration of Cr^{+3} which is due to concentration quenching, already described in Ref. 34. An analysis of the position of the luminescence signal reveals no shift of the double peak with increasing Cr^{3+} concentration in the $(AlCr)_2O_3$ material. Thus, the local coordination environment of Cr^{3+} (Cr–O distances) is equal for all samples and no clustering of Cr^{3+} inside the corundum phase is to be expected for the samples with higher Cr^{3+} content.

For all foam sample series, a pXRD and Rietveld characterization of the mortared $(AlCr)_2O_3$ foam strut material revealed the presence of only one single corundum phase with respect to an analysis of the reflection profiles (Figure 8).
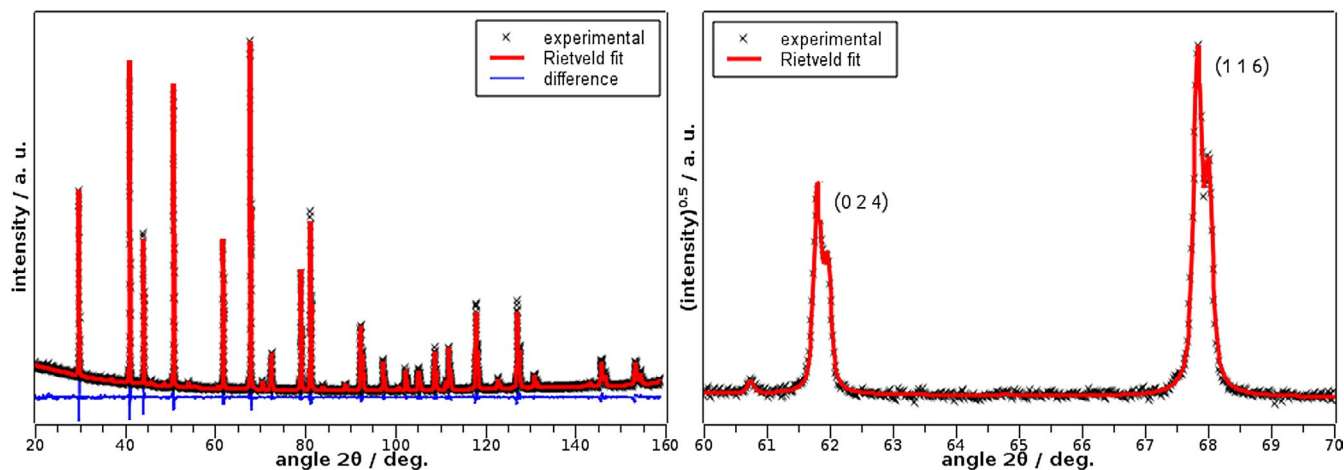
FIGURE 8 pXRD measurement and Rietveld analysis for an $(AlCr)_2O_3$ foam with 2.5 at.% Cr^{3+} sintered at 1650°C (left). The detail plot (right) shows no splitting of the reflections, thus only one corundum phase containing all Cr^{3+} is present

Consequently, a homogeneous $(AlCr)_2O_3$ solid solution has formed for all samples. According to the Al_2O_3-Cr_2O_3 phase diagram (Figure 1), this was expected, as the sintering temperature of 1650°C is clearly above the miscibility gap for all Cr^{3+} concentrations. The diffusion of Cr^{3+} and Al^{3+} inside the oxide phase is sufficiently fast at 1650°C.[32] Thus, a homogeneous distribution of Cr^{3+} was reached and no chromium gradient evolves, which would result in splitting of the corundum reflections in the pXRD pattern.

With respect to the Cr^{3+} concentration in the strut material of the foams after sintering, as determined from the pXRD data, no difference in the starting powders was observed (Table 3). Thus, a Cr depletion in the samples due to the formation of volatile Cr-O species during sintering can be excluded.

The sintering behavior of the $(AlCr)_2O_3$ foams is affected by the Cr^{3+} concentration in the strut material (Figure 9). With increasing Cr^{3+} content, the linear (and volumetric) shrinkage increases from 14% (43%) for pure alumina foams to 20% (55%) for the Al_2O_3-F-2.5 series. For the samples with the highest Cr^{3+} content of 5.0 mol% a decrease in shrinkage was observed again. This course in shrinkage is also reflected in a slight decrease in the cell size of the foams (alumina: 2.8 mm, Al_2O_3-F-1.25/2.5: 2.7 mm; Table 4).

This is in accord with the course of the total porosity of the foam samples, which decreases linearly from 90.4% for pure alumina to 87.9% for the Al_2O_3-F-2.5 series (Table 4, Figure 10). Higher Cr^{3+} concentrations do not result in a further decrease in porosity. With respect to the porosity inside the strut material no significant effect of the Cr^{3+} doping became apparent. The total strut porosity ranges between 18% and 20% for all sample series (Figure 10, Table 4). Thus, the effect of Cr^{3+} on the total porosity of the samples as discussed above is a consequence of the increased shrinkage and therefore the volume reduction of the foam samples.
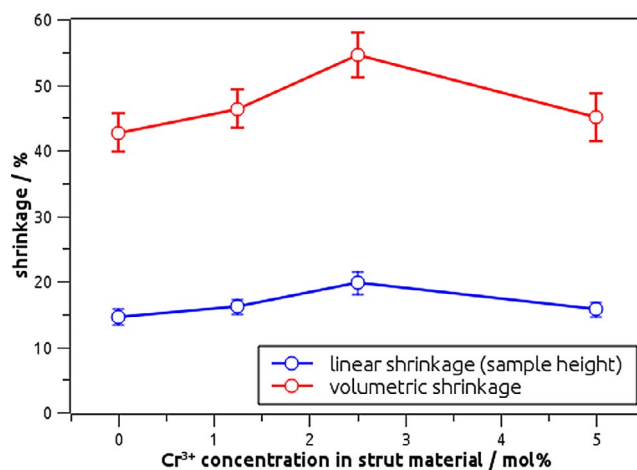

FIGURE 9 Linear and volumetric shrinkage behavior of alumina and $(AlCr)_2O_3$ foams as a function of the Cr^{3+} concentration within the strut material

In the literature, the densification behavior of Al_2O_3-Cr_2O_3 solid solutions has been investigated for bulk specimens.[35–38] Usually, an increasing Cr^{3+} content in the samples resulted in a decrease in densification and shrinkage and the formation of residual porosity. This has been accounted for by the vaporization/condensation of Cr_2O_3 and the additional thermal energy necessary for the diffusion-driven formation of the $(AlCr)_2O_3$ solid solution.[39] Both effects result in an increase in porosity as well as reduced densification and suit well as an explanation for the behavior of the Al_2O_3-F-5.0 samples. However, the increase in shrinkage and the corresponding porosity reduction of the Al_2O_3-F-1.25 and Al_2O_3-F-2.5 samples, respectively, have not been expected and do not fit into this context. Nevertheless, it should be noted that former sintering studies of Al_2O_3–Cr_2O_3 ceramics were focused on samples containing higher amounts of Cr^{3+},

TABLE 4 Compressive strength, total, and strut porosity and cell size (μ-CT) of the $(AlCr)_2O_3$ foams

Sample	Total por. / %	Strut por. / %	Cell size (CT) / mm	Compressive strength / MPa	Weibull modulus m
Al_2O_3-F-0	90.4 ± 0.5	19 ± 1.8	2.8 ± 0.1	0.79	4.0
Al_2O_3-F-1.25	89.2 ± 0.9	20 ± 1.5	2.7 ± 0.2	0.59	3.7
Al_2O_3-F-2.5	87.9 ± 1.4	20 ± 1.8	2.7 ± 0.2	0.76	3.4
Al_2O_3-F-5.0	88.0 ± 1.7	18 ± 1.7	--	0.56	1.8

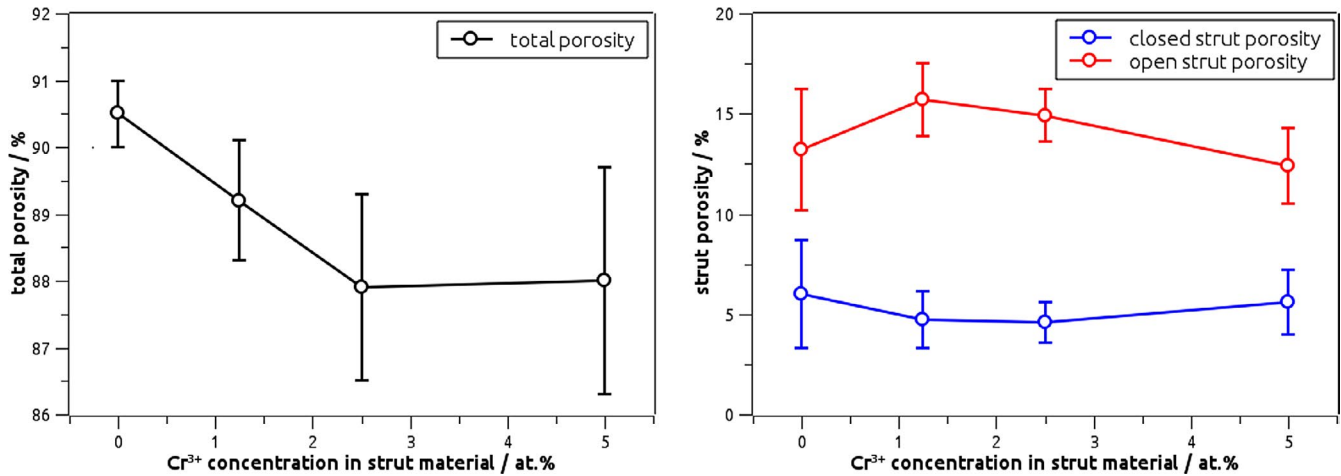**FIGURE 10** Total geometric porosity of alumina and $(AlCr)_2O_3$ foams after final sintering at 1,650°C as a function of the Cr^{3+} concentration within the strut material (left); open and closed strut material porosity (right)

in the first instance and no data for samples with Cr_2O_3 concentrations below 10 mol% exist. Most likely, other processes and reactions are effective for the samples with 1.25 mol% and 2.5 mol% Cr^{3+} within this study, which require additional investigation. Furthermore, the role of a highly porous cellular structure with a significantly increased specific surface to bulk volume ratio compared to bulk/dense ceramic parts remains unclear as well. Most likely, this is relevant with respect to the vaporization/condensation mechanism of Cr_2O_3 and needs additional investigation as well.

In order to evaluate the compressive strength data of the $(AlCr)_2O_3$ foams, the measured data were compared with alumina reference foams taken from the literature.[16] For this, the Al_2O_3 reference data were fitted with the Gibson–Ashby relation for brittle, cellular structures (Equation 2, Ref. 40) in order to get a measure of the significant effect of porosity on the mechanical strength:

$$\sigma_{cf} = C \cdot \left(\rho_{rel} \right)^n \cdot \sigma_{fs} \qquad (2)$$

The actual modeling of the strength data was performed using the linearized form of the Gibson–Ashby model (Equation 3) and a double-logarithmic plot of the compressive strength (σ_{cf}) and relative density data ($\rho_{rel} = 1-P$; P: total porosity). This approach allows a common linear regression analysis[16]:
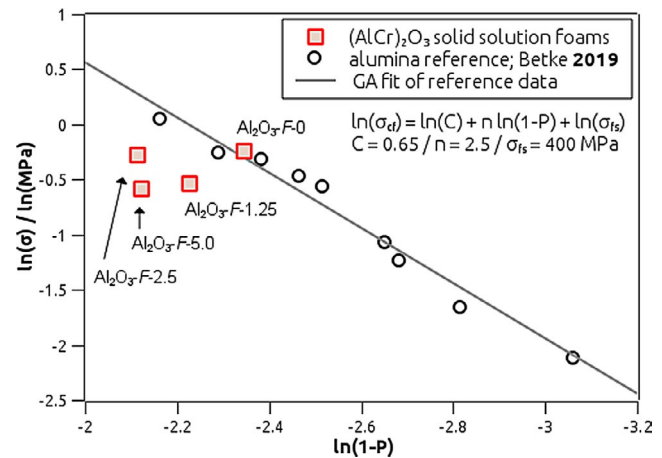

FIGURE 11 Gibson–Ashby (GA) plot of compressive strength data for pure alumina and $(AlCr)_2O_3$ foams as a function of total porosity (P). Data of plain alumina foams (gray) were obtained from Ref. 16 The regression line corresponds to the linearized Gibson–Ashby model with a density exponent n of 2.5, a geometry constant C of 0.65 and a bending strength of pure alumina of 400 MPa

$$\ln \left(\sigma_{cf} \right) = \ln \left(C \right) + n \cdot \left(\rho_{rel} \right) + \ln \left(\sigma_{fs} \right) \qquad (3)$$
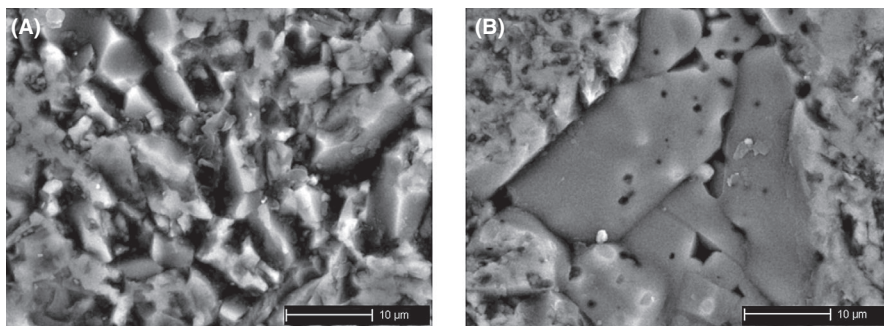
FIGURE 12 SEM micrograph of a cross-section of the pure alumina strut material (A) and a $(AlCr)_2O_3$ foam containing 2.5 mol% Cr^{3+} (B). For the latter, significant grain growth is found

For the geometry parameter C, a literature value of 0.65 was used according to Ref. 40 and the density exponent n was set to 2.5 in agreement with previous studies of brittle cellular ceramics.[16,41–43] Furthermore, a bending strength of $\sigma_{fs} = 400$ MPa for alumina in accord with literature data was used.[2] Finally, using Equation 3, the compressive strength of an alumina foam with the same total porosity like the respective $(AlCr)_2O_3$ sample can be calculated for a direct comparison.

The compressive strength of the $(AlCr)_2O_3$ foams is significantly lower compared to pure alumina foams (Figure 11, Table 4). For the Al_2O_3-F-1.25 and Al_2O_3-F-2.5 foams, σ_{cf} is reduced by 42%, on average compared to alumina foams at the same porosity level. For the Al_2O_3-F-5.0 samples, the decrease in strength is more pronounced with 57% compared to alumina. The course of the strength results is in line with the Weibull modulus m of the foam samples. The Weibull modulus decreases from $m = 4.0$ for samples without Cr^{3+} to only 1.8 for the Al_2O_3-F-5.0 foams indicating a large variation of the compressive strength data.

The decrease in strength for Al_2O_3-Cr_2O_3 ceramics with increasing Cr^{3+} concentration has been observed for bulk ceramic parts as well,[38] at least for higher Cr^{3+} contents of 10 mol% and above. The reason for this is an increase in the growth rate of the alumina crystallites promoting grain growth.[44] In the finally coarsened microstructures of Cr-rich Al_2O_3–Cr_2O_3 ceramics, strength is lowered due to increased crack propagation. For the Cr-doped foam samples, significant grain growth has been observed (Figure 12), which might contribute to the lowering of the mechanical strength. Nevertheless, for very low chromium doping levels in the order of 0.5 vol%, which is 0.45 mol%, an increase in the bending strength as well as the fracture strength of the obtained Al_2O_3–Cr_2O_3 composites has been reported.[39,45] The reason for this is a grain-boundary effect: The larger Cr^{3+} ions generate localized compressive stress at the grain boundaries which effectively hinders crack penetration. This phenomenon might contribute to the higher compressive strength of the Al_2O_3-F-1.25 and Al_2O_3-F-2.5 samples compared to the Al_2O_3-F-5.0 samples. However, for the latter, the positive grain-boundary effect of Cr^{3+} is overlapped by the negative effects of an increased grain growth.

In summary, the mechanical properties of (cellular) Al_2O_3-Cr_2O_3 ceramics are determined by several effects, which are governed by the amount of Cr^{3+} ions incorporated in the respective corundum phase. For the foam samples within this work, however, no positive effect of Cr^{3+} doping has been observed. The compressive strength of $(AlCr)_2O_3$ foams is 40% to 60% lower compared to that of pure alumina foams with the same porosity level.

4 | CONCLUSIONS

Open cellular ceramic foams were manufactured from undoped and Cr^{3+}-doped alumina powders; doping of the starting powders was carried out by a precipitation process of the chromia precursor compound $(NH_4)Cr(OH)_2(CO_3)$ on the surface of an alumina ceramic powder. The doping with Cr^{3+}—related to the incorporation into the alumina lattice—was adjusted between 1.25 mol% and 5.0 mol%, respectively. The calcination of these powders at 1,000°C lead to a partial incorporation of Cr^{3+} in the alumina lattice. However, Cr^{3+} was completely dissolved in a homogeneous $(AlCr)_2O_3$ solid solution with corundum structure during sintering of the foams at 1,650°C for all Cr^{3+} concentrations.

Chromium incorporation influenced the sintering behavior and the total foam porosity, respectively. Doping with Cr^{3+} led to a significant reduction of the total porosity due to an increased sintering activity and more pronounced shrinkage: While undoped samples possess a porosity of 90.4%, the porosity of doped samples was in the range between 88% and 89% depending on the Cr^{3+} concentration. The strut porosity in the foams is influenced by Cr^{3+} doping less significantly. Thus, the porosity reduction with increasing Cr^{3+} content is mainly driven by the increased shrinkage.

The compressive strength of the $(AlCr)_2O_3$ foams is lower than the strength of pure alumina samples—at least when the specimens are compared at the same total porosity level.

In summary, it can be concluded that the manufacturing of chromia-alumina foams is possible. Even if there was no increase in the compressive strength, doping with Cr^{3+} may be a tool for the control of the porosity in cellular ceramics by adjustment of the material's shrinkage.

ORCID
Ulf Betke https://orcid.org/0000-0001-8896-8283
Michael Scheffler https://orcid.org/0000-0001-5509-1868

REFERENCES
1. Fey T, Betke U, Rannabauer S, Scheffler M. Reticulated replica ceramic foams: processing, functionalization, and characterization. Adv Eng Mater. 2017;19:1700369.
2. Studart AR, Gonzenbach UT, Tervoort E, Gauckler LJ. Processing routes to macroporous ceramics: a review. J Am Ceram Soc. 2006;89:1771–89.
3. Olson RA, Martins LCB. Cellular ceramics in metal filtration. Adv Eng Mater. 2005;7:187–92.
4. Twigg MV, Richardson JT. Fundamentals and applications of structured ceramic foam catalysts. Ind Eng Chem Res. 2007;46:4166–77.
5. Betke U, Lieb A. Micro-macroporous composite materials - preparation techniques and selected applications: a review. Adv Eng Mater. 2018;20:1800252.
6. Schelm K, Fey T, Dammler K, Betke U, Scheffler M. Hierarchical-porous ceramic foams by a combination of replica and freeze technique. Adv Eng Mater. 2019;21:1801362.
7. Dammler K, Schelm K, Betke U, Fey T, Scheffler M. Open-cellular alumina foams with hierarchical strut porosity by ice templating: a thickening agent study. Materials. 2021;14:1060.
8. Voigt C, Jäckel E, Aneziris CG, Hubálková J. spinel coating on alumina foam ceramics for aluminum filtration. Adv Eng Mater. 2013;15:1197–205.
9. Storti E, Farhani M, Aneziris CG, Wöhrmeyer C, Parr C. Calcium aluminate reactive coatings on carbon-bonded alumina filters for clean steel approaches. Steel Res Int. 2017;88:1700247.
10. Betke U, Klaus M, Eggebrecht JG, Scheffler M, Lieb A. MOFs meet macropores: dynamic direct crystallization of the microporous aluminum isophthalate CAU-10 on reticulated open-cellular alumina foams. Microporous Mesoporous Mater. 2018;265:43–56.
11. Bauer C, Scheffler F, Schwidder M. Direct crystallization of silicoaluminophosphates onto the surface of open-celled SiC foam. Adv Eng Mater. 2015;17:656–62.
12. Vogt UF, Gorbar M, Dimopoulos-Eggenschwiler P, Broenstrup A, Wagner G, Colombo P. Improving the properties of ceramic foams by a vacuum infiltration process. J Eur Ceram Soc. 2010;30:3005–11.
13. Chen X, Betke U, Rannabauer S, Peters PC, Söffker GM, Scheffler M. Improving the strength of ZTA foams with different strategies: immersion infiltration and recoating. Materials (Basel). 2017;10:735.
14. Liang X, Li Y, Liu J, Sang S, Chen Y, Li B, et al. Fabrication of SiC reticulated porous ceramics with multi-layered struts for porous media combustion. Ceram Int. 2016;42:13091–7.
15. Rannabauer S, Söffker G-M, Scheunemann M, Betke U, Scheffler M. Increased mechanical stability and thermal conductivity of alumina reticulated porous ceramics (RPC) by nanoparticle infiltration processing. Adv Eng Mater. 2017;19:201700211.
16. Betke U, Scheunemann M, Scheffler M. Refitting of zirconia toughening into open-cellular alumina foams by infiltration with zirconyl nitrate. Materials. 2019;12:1886.
17. Fujita M, Inukai K, Sakida S, Nanba T, Ommyoji J, Yamaguchi A, et al. Sintering of Al_2O_3-Cr_2O_3 powder prepared by sol-gel process. J Soc Mat Sci. 2007;56:526–30.
18. Shannon RD. Revised effective ionic radii and systematic studies of interatomic distances in halides and chalcogenides. Acta Cryst A. 1976;32:751–67.
19. Holleman AF, Wiberg N. Lehrbuch der anorganischen Chemie. 102. Aufl. Berlin: De Gruyter; 2007.
20. Lange FF. Transformation toughening: part 1 size effects associated with the thermodynamics of constrained transformations. J Mater Sci. 1982;17:225–34.
21. Lange FF. Transformation toughening: Part 2 Contribution to fracture toughness. J Mater Sci. 1982;17:235–9.
22. Lange FF. Transformation toughening: part 3 experimental observations in the ZrO_2 - Y_2O_3 system. J Mater Sci. 1982;17:240–6.
23. Lange FF. Transformation toughening: part 4 fabrication, fracture toughness and strength of Al_2O_3 - ZrO_2 composites. J Mater Sci. 1982;17:247–54.
24. Schwartzwalder K, Somers H, Somers AV. Method of making porous ceramic articles. US 3,090,094. 1961.
25. Lafficher R, Digne M, Salvatori F, Boualleg M, Colson D, Puel F. Ammonium aluminium carbonate hydroxide $NH_4Al(OH)_2CO_3$ as an alternative route for alumina preparation: Comparison with the classical boehmite precursor. Powder Technol. 2017;320:565–73.
26. Betke U, Proemmel S, Rannabauer S, Lieb A, Scheffler M, Scheffler F. Silane functionalized open-celled ceramic foams as support structure in metal organic framework composite materials. Microporous Mesoporous Mater. 2017;239:209–20.
27. Rossi LR, Lawrence WG. Elastic properties of oxide solid solutions: the system Al_2O_3–Cr_2O_3. J American Ceramic Society. 1970;53:604–8.
28. Advanced technical ceramics; monolithic ceramics; general and textural properties; part 2: determination of density and porosity; German version EN 623-2:1993.
29. Betke U, Dalicho S, Rannabauer S, Lieb A, Scheffler F, Scheffler M. Impact of slurry composition on properties of cellular alumina: a computed tomographic study. Adv Eng Mater. 2017;19:1700138.
30. Ronninger C. Visual-XSel 14. Starnberg, Germany: CRGRAPH; 2018.
31. Vegard L. Die Konstitution der Mischkristalle und die Raumfüllung der Atome. Z Phys. 1921;5:17–26.
32. Suzuki AM, Yasuda A, Ozawa K. Cr and Al diffusion in chromite spinel: experimental determination and its implication for diffusion creep. Phys Chem Minerals. 2008;35:433–45.
33. Zuo C, Jagodzinski PW. R-line luminescence from trace amounts of Cr^{3+} in aluminum oxide and its dependence on sample hydration. Appl Spectrosc. 2002;56:1055–8.
34. Zhou J, Xia Z. Synthesis and near-infrared luminescence of $La_3GaGe_5O_{16}$:Cr^{3+} phosphors. RSC Adv. 2014;4:46313–8.
35. Cho S-A, Arenas FJ, Ochoa J. Densification and hardness of Al_2O_3–Cr_2O_3 system with and without Ti addition. Ceram Int. 1990;16:301–9.
36. Hirata T, Akiyama K, Yamamoto H. Sintering behavior of Cr_2O_3–Al_2O_3 ceramics. J Eur Ceram Soc. 2000;20:195–9.
37. Nath M, Kumar P, Maldhure AV, Sinhamahapatra S, Dana K, Ghosh A, et al. Anomalous densification behavior of Al_2O_3–Cr_2O_3 system. Mater Charact. 2016;111:8–13.
38. Cui K, Zhang Y, Fu T, Hussain S, Saad Algarni T, Wang J, et al. Effects of cr_2o_3 content on microstructure and mechanical properties of Al_2O_3 matrix composites. Coatings. 2021;11(2):234.

BETKE ET AL.

Applied
Ceramic
International Journal of
TECHNOLOGY

199

39. Kafkaslıoğlu Yıldız B, Yılmaz H, Tür YK. Evaluation of mechanical properties of Al_2O_3–Cr_2O_3ceramic system prepared in different Cr_2O_3 ratios for ceramic armour components. Ceram Int. 2019;45:20575–82.

40. Ashby MF, Mehl-Medalist RF. The mechanical properties of cellular solids. Metall Trans A. 1983;14:1755–69.

41. Costa Oliveira FA, Dias S, Fátima Vaz M, Cruz Fernandes J. Behaviour of open-cell cordierite foams under compression. J Eur Ceram Soc. 2006;26:179–86.

42. Sousa E, Rambo CR, Hotza D, Novaes de Oliveira AP, Fey T, Greil P. Microstructure and properties of LZSA glass-ceramic foams. Mater Sci Eng, A. 2008;476:89–97.

43. Betke U, Schelm K, Rodak A, Scheffler M. Cellular nickel-yttria/zirconia (Ni–YSZ) cermet foams: manufacturing, microstructure and properties. Materials. 2020;13:2437.

44. Harabi A, Davies T. Effect of chromia on grain growth in alumina. MSF. 1992;94–96:797–802.

45. Li CL, Riu DH, Sekino T, Niihara K. Fabrication and mechanical properties of Al_2O_3 solid solution with low addition of Cr_2O_3. KEM. 1998;161–163:161–4.